Supplementary information

for

Growth laws for channel networks incised by groundwater flow

Daniel M. Abrams[1], Alexander E. Lobkovsky[1], Alexander P. Petroff[1], Kyle M. Straub[1*], Brandon McElroy[2], David C. Mohrig[2], Arshad Kudrolli[3], and Daniel H. Rothman[1]

[1]*Department of Earth, Atmospheric and Planetary Sciences, Massachusetts Institute of Technology, Cambridge, MA 02139 USA*
[2]*Department of Geological Sciences, University of Texas at Austin, Austin, TX 78712 USA*
[3]*Department of Physics, Clark University, Worcester, MA 01610 USA*
[*]*Present address: Department of Earth and Environmental Sciences, Tulane University, New Orleans, LA 70118 USA*

Contents

1   Supplementary video legends

1.1   Supplementary Video Legend 1

This movie shows the backwards evolution of the Florida network. Each colored polygon represents the geometric drainage area associated with the nearest channel head. The speed at which channels are retracted is proportional to this area. Note especially the simultaneous retraction of bifurcated channels to the original, unsplit, channel heads. Although we cannot be certain of the origin of all channel heads, the occurrence of such tip-splitting events at all times suggests that the backwards evolution is broadly correct.

1.2   Supplementary Video Legend 2

This movie reconstructs the forward evolution of the Florida network. It contains the same information as Supplementary Video 1, but without the colored drainage areas. Note that the precise time of the birth of new channels by tip-splitting and side-branching must be obtained from the backwards evolution of Video 1.

2   Images of the field site

The valleys containing the Florida channels are typically about 60–100 m wide and 20–30 m deep, with steeply sloped (30–40 degrees) sides cut into a relatively flat plain. Figure S1 shows a typical valley sidewall descending from the plain. Figure S2a is a photograph of a valley head, looking upward from its base. Figure S2b shows a typical active spring at the base of a valley head.

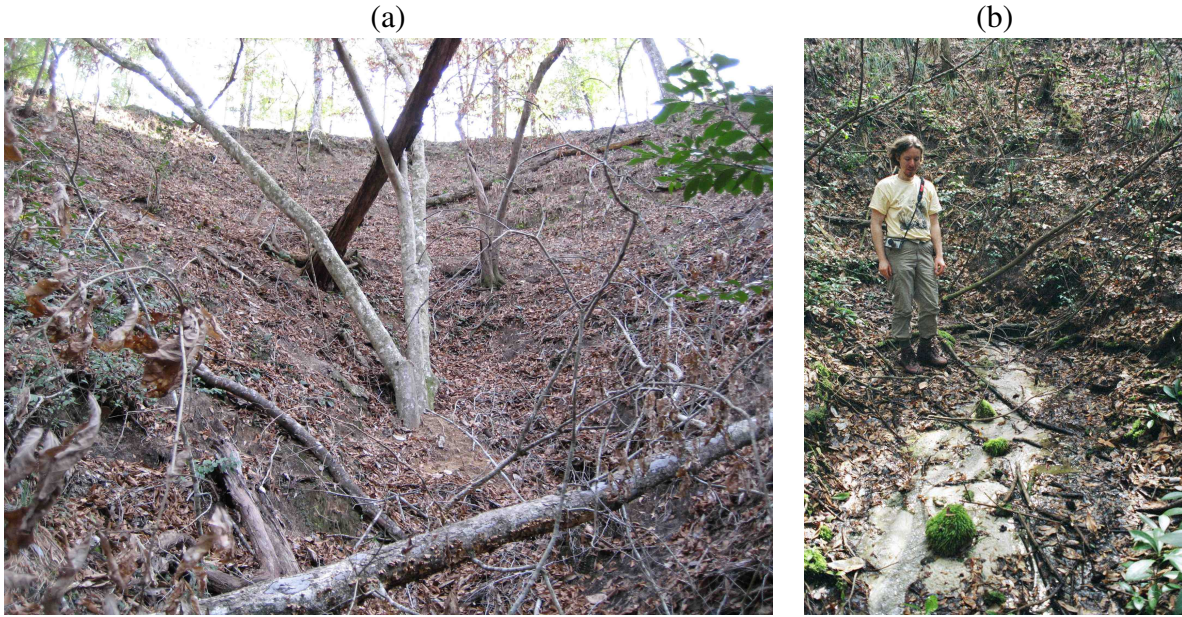Figure S1: Sidewall of a valley descending leftwards from the flat plain.

Figure S2: (a) A valley head, looking upwards from above its base. Note the nearly circular lip at top. (b) A spring emerges at the base of a valley head, adjacent to the observer's left foot.

3 Ground penetrating radar survey of the water table

3.1 Data collection and processing

The map of the water table shown in Figure 2 of the main text was obtained by a three-dimensional Ground Penetrating Radar (GPR) survey along the transects shown in Figure S3. The survey was conducted with a Geophysical Survey Systems 100 MHz bistatic radar antenna. This GPR system allows for accurate imaging of 50 m of the stratigraphy beneath a unit when well coupled to the ground surface and penetrating through fine to coarse sand.

Collection of data occurred while the GPR unit was towed behind a four-wheel-drive automobile (Figure S4). The unit was towed on transects that were cleared of vegetation and recently plowed. Most transects followed a southeast to northwest orientation with occasional transects oriented to act as cross-lines in the survey. Collection of data occurred while the GPR unit moved at a speed between 0 and 15 km/hr. Individual vertical GPR profiles were 300 nanoseconds long and had a sampling interval of 0.1 nanoseconds. Separate GPR vertical profiles were collected at a frequency of 10 Hz while towed. The absolute spatial location of the GPR unit was obtained via time synchronization with a Trimble ProXH differential GPS receiver with a 0.30 m spatial resolution. This GPS receiver samples at a frequency of 1 Hz.

We processed the GPR data for each transect with a series of filters, beginning with raw data from the instrument's antenna. First we applied appropriate gain to the decaying signal proportional to time squared and filtered obvious noise. We then converted the uniformly-timed samples to uniform spacing along our transect, with the help of GPS positioning information that had been simultaneously collected. After that we filtered out high-frequency noise and noise from a faulty coaxial cable. After further deconvolving the instrument's input signal, we were able to produce
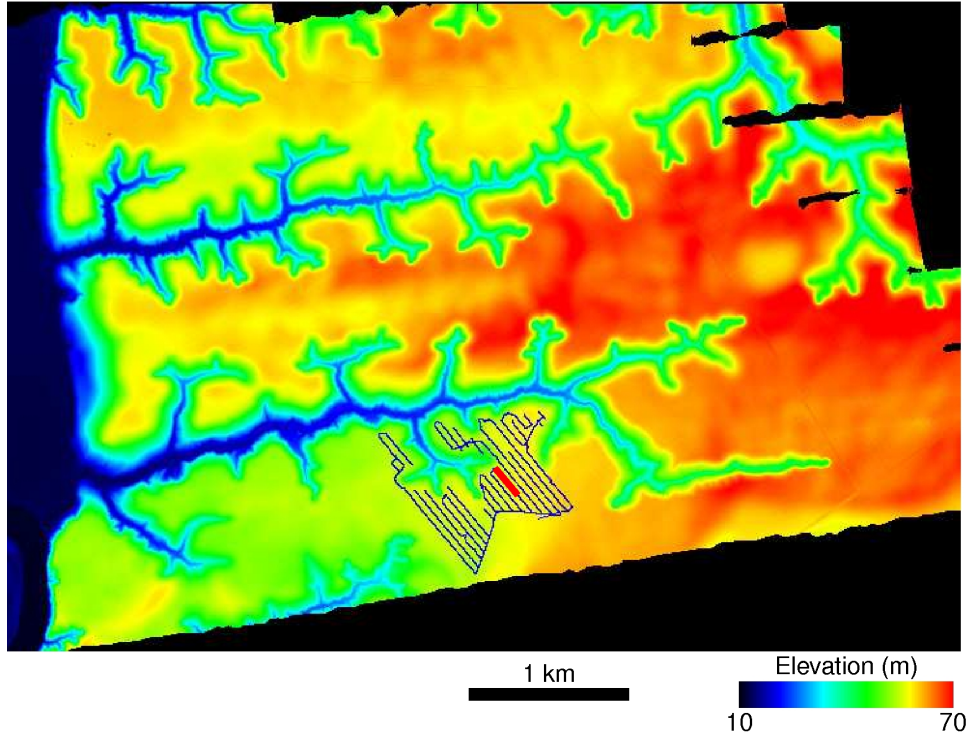
Figure S3: Location of GPR transects superimposed on the surface topography of the channel network. All transects are shown with thin blue lines, except one, shown in thick red, which corresponds to the location of the GPR data shown in Figure S5.

an almost-visual representation of the subsurface.

We also "migrated" the data, using a frequency-domain Stolt algorithm [S1], on selected lines in which hyperbolic diffraction patterns obscured the image. This step also allowed us to estimate the average dielectric constant or relative static permittivity ($\varepsilon_r \simeq 12$) of the subsurface by finding the wave speed for which migration optimally collapsed diffracted waves, thus allowing us to convert reflection time to depth. In order to establish the height of the water table above sea level, we first converted our depth scale to elevation by combining data from the instrument's horizontal GPS positioning and our high-resolution (1-m) topographic map.

The processed GPR data was then imported into a three-dimensional seismic interpretation software package commonly used for seismic reflection surveys in the petroleum industry. Individual transects were positioned with resampled GPS data. Due to the homogeneous nature of the sediment, few subsurface impedance horizons exist with lateral extents greater than 20 meters. The water table on each transect was therefore manually identified as the depth where scattered waves disappear.

This final step is illustrated by Figure S5, which shows a representative example of the processed GPR data. We interpret the transition from strongly scattered waves to a weak or non-existent signal as resulting from the lack of significant reflectors (i.e., contrasts in the dielectric constant) in fully saturated wet sand. Unfortunately, the transition was not always associated with a sharp transition from high to low amplitude regions, making automated identification of the water table difficult. We therefore manually picked 1065 water table elevations at individual x, y

S4

Figure S4: Configuration for the ground-penetrating radar survey. A 100 MHz bistatic radar antenna manufactured by Geophysical Survey Systems, Inc., was towed behind an automobile with an operator trailing the antenna and controlling the instrument with portable laptop.

locations. The map of the water table elevation (Figure 2a of the main test) was created by spatial interpolation of the elevation data with an ordinary "kriging" method, resulting in a uniformly spaced grid with 5-m resolution.

3.2   Analysis of water table shape

Figure 2b of the main text shows the 1065 elevation picks as a function of their horizontal distance to the nearest channel (approximated by the 30-m contour). The theoretical curve fit to these data is the Dupuit-Forchheimer ellipse [S2]. This requires the assumptions that the flow is primarily horizontal and directed toward the nearest channel.

For completeness, we review here some elements of the theory [S2]. In a one dimensional model system at equilibrium with rain falling on the surface at rate r, the net horizontal seepage flux Q at a distance x from the groundwater divide must be $Q(x) = rx$ (conservation of mass). This must be equivalent to the vertically integrated flux $Q = qh$, where h is the height of the column of groundwater measured from a base layer and q is the specific discharge, given by Darcy's law as $q = -K \sin \theta$. Here K is the hydraulic conductivity and θ is the angle of the surface of the groundwater table, which can be approximated for small θ as dh/dx. Thus
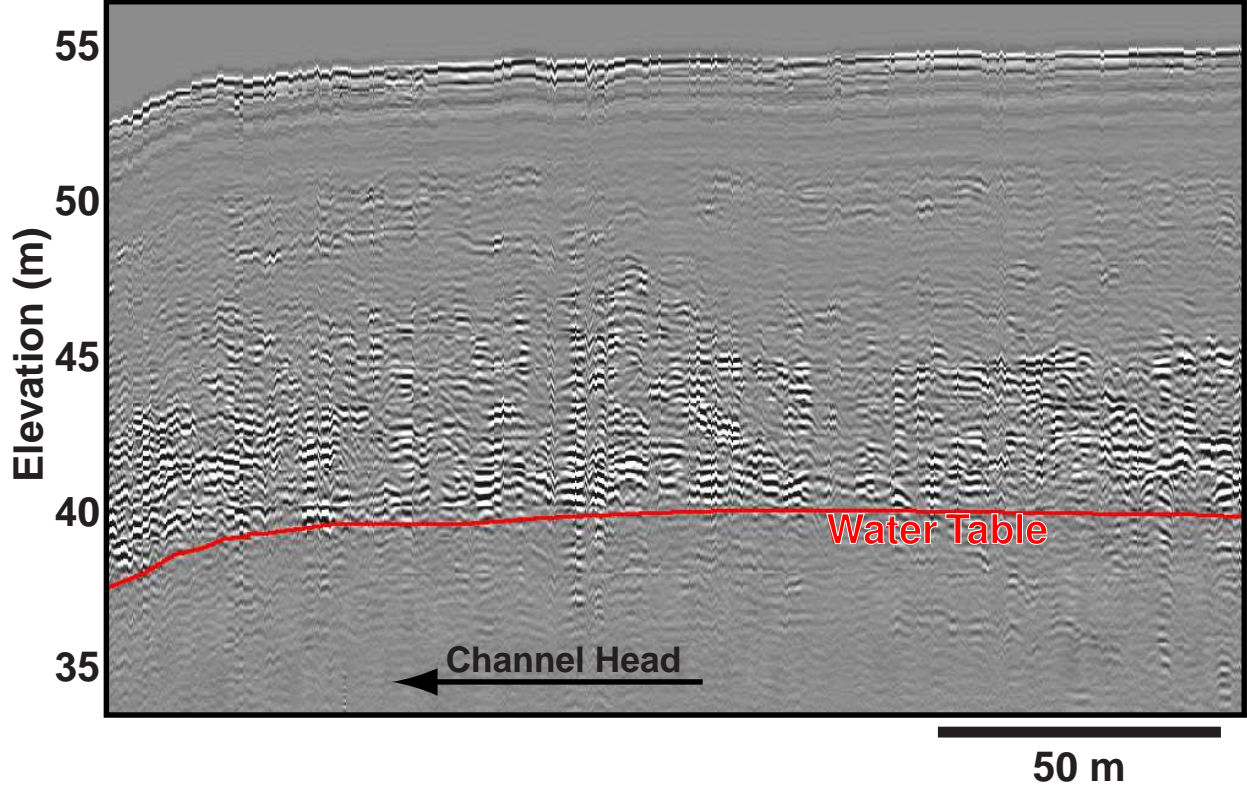
$$Q = rx = -Kh\frac{dh}{dx} \; ,$$

Figure S5: A representative example of processed two-dimensional GPR data, obtained on the transect shown as the thick red line in Figure S3. The location of the water table is interpreted as the base of the region with highly scattered waves.

which has for its solution the ellipse

$$h(x)^2 = -\frac{r}{K}x^2 + C \, . \tag{S1}$$

To fit the Dupuit-Forchheimer ellipse (S1) to the water table data, we use least-squares regression with two free parameters corresponding to the semi-major and semi-minor axes of the ellipse. The ellipse's center coordinates are determined by the assumptions that *i*) the ellipse is vertically tangent at the spring position, and *ii*) the y-coordinate of the ellipse's center is the mean measured spring elevation (35.1m).

The resulting best-fit ellipse has a semi-minor axis $x_1 = 6.6$ m and a semi-major axis $x_2 = 465$ m, which implies that the ratio $r/K = x_1^2/x_2^2 \approx 2 \times 10^{-4}$. Recent historical rainfall rates in Bristol, FL (approximately 0.4 cm/day) yield an estimated $r \sim 5 \times 10^{-8}$ m/s, implying a hydraulic conductivity $K \sim 3 \times 10^{-4}$ m/s. This estimated value is consistent with typical hydraulic conductivities for clean sand [S2] and our own field measurements.

Finally, we note that the large spread of the data in Figure 2b may be partially explained by the presumably wide distribution of distances to the drainage divides in various parts of the surveyed region.

4 Geometric approximation of the flux to channel tips

In this section we show that the geometric drainage area a (see main text) associated with a channel tip is approximately proportional to the flux to the tip predicted by numerical simulation of three-dimensional groundwater flow. We begin by detailing our numerical computation of the water table shape for the case of a channel side-branch of length ℓ connected to a main stream. The steady-state flux to the channel tip is then obtained from the subsurface area a' that contains the groundwater flow draining into the tip. We next provide an explicit expression for the geometric area a in the same system. Finally, we show that, to good approximation, $a(\ell) \propto a'(\ell)$.

4.1 Computation of the water table shape and the subsurface area a'

We numerically compute the fully 3D steady-state water table recharged by steady rain. Fig. S6a shows an example of the surface topography in the computational domain. The water drains into a periodic array of parallel V-shaped main channels separated by a distance $2H$. The main channels contain side-branches of length $\ell < H$. These side-branches are normal to the main channels. There is mirror symmetry across the divide between the main channels so that each side-branch faces another side-branch growing from the next main channel, with the groundwater divide always at a distance H between the two main channels. The distance between side-branches along the main channel is sufficiently large to ignore interactions. The side-branch terminates in a conical head with the slope of the side walls.

Our physical assumptions are as follows:

- The rain falls steadily at rate r.

- The sand is homogeneous with hydraulic conductivity K.

- The infiltration rate is sufficiently large such that the overland flow is negligible.

- All rainwater drains into the channels from the subsurface.

- Water seeping into the channels through the side-walls is immediately removed. This assumption is needed for the atmospheric pressure boundary condition at the seepage face (the region where the water table intersects a channel side-wall).

The height $h(x, y)$ of the water table, defined at horizontal coordinates x and y, is found by solving a moving boundary problem (e.g., Refs. [S2, S3]). The reduced pressure

$$\Pi(x, z) = \frac{p}{\rho g} \tag{S2}$$

obeys Laplace's equation

$$\nabla^2 \Pi = 0 \tag{S3}$$

beneath the water table. Here Π has the dimension of length, ρ is the density of water, and g is the acceleration of gravity. From Darcy's law, the dimensionless seepage velocity is

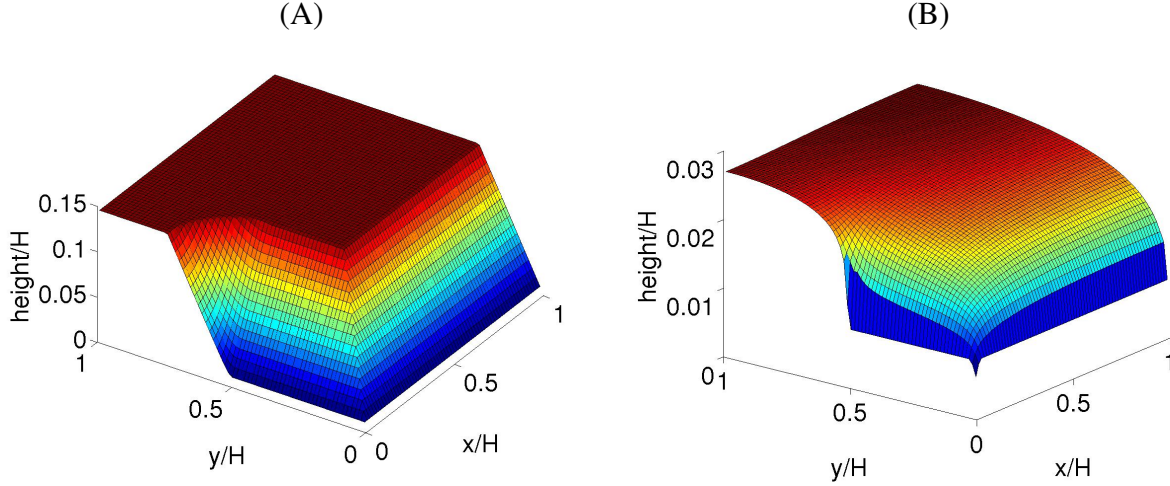$$\vec{v}(x, z) = -\vec{\nabla}\Pi - \hat{\mathbf{z}}, \tag{S4}$$

Figure S6: (a) Surface topography overlying the steady-state water table. A flat plain (top) is cut by the main, throughgoing, channel (parallel to the x-axis) and a side-branch (parallel to the y-axis) with a conical channel head. Mirror symmetry is imposed at $x = H$ and $y = H$. (b) Calculated geometry of the steady-state water table, for $r/K = 0.01$. The height in both plots is referenced to the same datum.

where $\hat{\mathbf{z}}$ is the unit vector up in the vertical direction.

Laplace's equation is solved in a domain which is bounded by the following: $x = 0$: a vertical plane bisecting the side-branch; $y = 0$: a vertical plane bisecting the main channel; $y = H$: a vertical plane at the main channel divide; $x = H$: a vertical plane parallel to the side-branches at the mid-point between the side-branches; top: the water table; and bottom: a flat horizontal, sufficiently deep, impermeable surface where the subsurface flows vanish.

Except at the water table, the boundary conditions are the vanishing normal seepage velocity, $\hat{\mathbf{n}} \cdot \vec{v} = \hat{\mathbf{n}} \cdot \nabla\Pi = 0$, either due to symmetry or impermeability at the boundary perpendicular to the unit normal $\hat{\mathbf{n}}$. At the water table, the pressure is atmospheric ($\Pi = 0$) by definition. At the seepage face, i.e. where the water table coincides with the channel's side wall, the location of the water table is known. To locate the water table elsewhere we need an extra condition provided by the requirement of water conservation. When the water table does not coincide with the side wall of a channel, its normal seepage velocity $K(\hat{\mathbf{n}} \cdot \vec{v})$ must be balanced by the normal velocity $r(\hat{\mathbf{n}} \cdot \hat{\mathbf{z}})$ due to the rainfall ($\hat{\mathbf{n}}$ is the upward unit normal to the water table). Thus, the extra condition at the water table is

$$K(\hat{\mathbf{n}} \cdot \vec{v}) - r(\hat{\mathbf{n}} \cdot \hat{\mathbf{z}}) = 0. \tag{S5}$$

The height of the water table for which equation (S5) holds is found iteratively. Given a guess of the water table height, we solve Laplace's equation via a relaxation method, with $\Pi = 0$ at the water table. For an incorrect guess of the water table height h, the left hand side of (S5) does not vanish, in general. The water table is then moved vertically by a small amount in such a way as to reduce size of the error in expression (S5). Since the amount by which the water table is moved is proportional to the discrepancy in (S5), iterating this procedure leads to the convergence of the water table to its true position for which (S5) holds everywhere along the water table (excluding the seepage face).
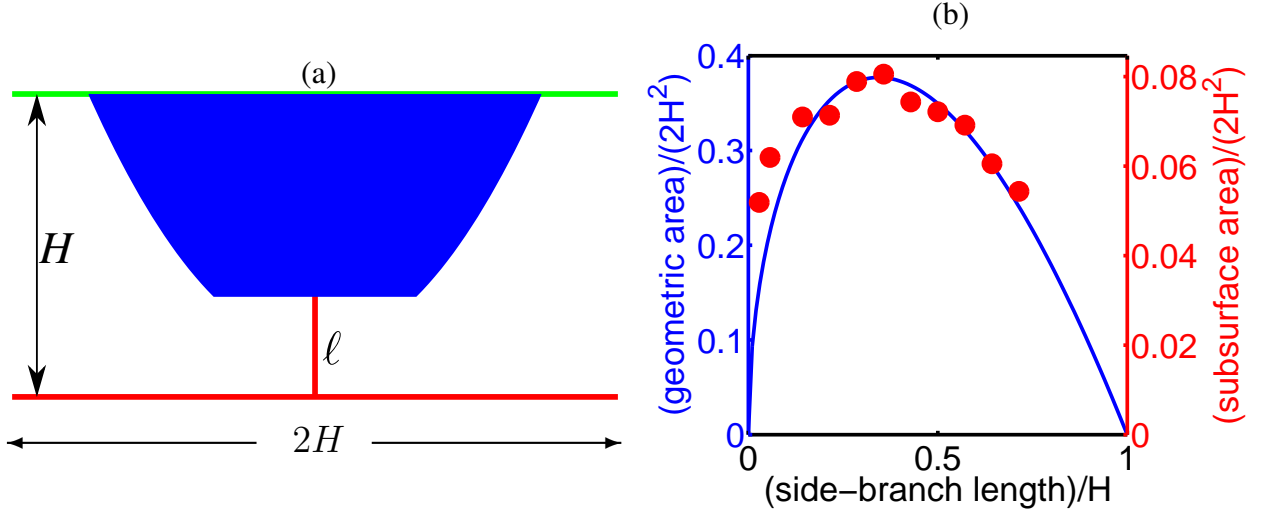
Figure S7: (a) The geometric drainage area (blue) associated with the tip of a channel side-branch of length ℓ (vertical red line). The side-branch drains in the main channel, represented by the horizontal read line. The upper green line is a fixed groundwater divide. (b) Comparison of the geometric drainage area a (smooth blue curve) calculated from equation (S7) to the subsurface area a' (red dots) obtained from numerical simulation of the full three-dimensional groundwater flow.

Given the seepage velocity in the steady state we seek the basin draining into the conical tip of the side-branch. To do so, we compile a two-dimensional map of the vertically integrated seepage velocity $\mathbf{V}_{2D}$. We then compute the two-dimensional streamlines that result from a projection $\mathbf{V}_{2D}$ onto the horizontal plane. The streamline that terminates at the apex of the conical head then delineates the basin that drains into the head of the side-branch. We denote this area by a' and refer to it as the *subsurface area*. Because all water that rains onto the surface above a' must flow into the head of the side-branch, a' is proportional to the flux to the channel head.

4.2   The geometric drainage area a and its comparison to a'

The *geometric drainage area* a associated with a channel tip is the area on the surface that is closer to the planform location of that channel tip than to any other point on the channel network. Figure S7a illustrates the geometric drainage area for the same geometry used for the water table computation, i.e., drainage into a side-branch of length ℓ attached to a main channel, with the groundwater divide a distance H from the main channel.

To calculate the geometric drainage area explicitly, consider an x, y plane whose origin is at the intersection of the side-branch with the main branch, so that the the channel tip is located at position $x = 0$, $y = \ell$. The part of the plane that is closer to the tip than to any other point on the network must simultaneously satisfy

$$y \geq \ell \qquad \text{and} \qquad y^2 \geq x^2 + (y - \ell)^2. \tag{S6}$$

The solid blue region of Figure S7a satisfies these inequalities precisely. After integration, we find

its area, the geometric drainage area $a(\ell)$:

$$a(\ell) = \frac{2\ell^{1/2}}{3} \left[(2H - \ell)^{3/2} - \ell^{3/2} \right]. \qquad (S7)$$

Figure S7b compares the geometric drainage area $a(\ell)$ to the subsurface area $a'(\ell)$ obtained from the numerical solution of the three-dimensional groundwater flow detailed above. Both $a(\ell)$ and $a'(\ell)$ have their maximum near $\ell = 1/3$. Additionally, both must rise from zero at $\ell = 0$ and fall back to zero at $\ell = 1$. The overall similar shape of the two functions suggests the approximate relation $a(\ell) \propto a'(\ell)$, with the geometric drainage area being roughly five times greater. This difference in magnitude implies that the geometric approximation overestimates the flux to tips compared to the flux to sidewalls. In other words, the "screening efficiency" S of equation (5) of the main text is roughly five times larger when fluxes are computed geometrically rather than hydrodynamically. However, because $a(\ell) \propto a'(\ell)$, the *relative* flux to a network's tips is well approximated by the relative size of the geometric drainage areas associated with each tip. This justifies our use of the geometric approximation in the main text.

In general, the comparison between a' and a should depend on the dimensionless forcing r/K used to calculate a'. For small r/K, however, the water table is nearly flat and flow is nearly horizontal. The Dupuit approximation then predicts that the seepage velocity is proportional to the gradient of a potential that satisfies a two-dimensional Poisson equation [S2]. We verified that our full three dimensional calculations correspond to the limit of small r/K by comparing its results to numerical solutions of Poisson's equation using the boundary conditions of Figure S7. The Poisson solution indeed yields nearly the same results as the full calculation, with the only difference being that its values of $a'(\ell)$ are about 10% larger.

Finally, we note that our two-dimensional geometric approximation assumes that all water enters the network at the same elevation. This neglect of the third dimension is justified by our imaging of the watertable, which suggests, as shown in Figure 2 of the main text, that water table elevation is largely determined by the horizontal distance to the nearest channel.

4.3 Physical interpretation

The limit of two-dimensional flow also provides a physical interpretation of the geometric drainage area. Consider a two-dimensional network on the plane. Now pick a particular point at location $\mathbf{r}$ on the plane, and imagine that $\mathbf{r}$ is a source of raindrops that diffuse on the plane until they are absorbed by the network. A superposition of such diffusion problems for all possible source locations is equivalent to the Poisson problem described above.

For a single source, the diffusion process may be modeled as a random walk in which the network represents absorbing sites [S4, S5]. For a steady supply of walkers (i.e., "raindrops") we seek the relative fraction that are absorbed at each site on the network. A calculation of this fraction for the entire network is a formidable problem [S4, S5]. However the network site that receives the largest number of walkers is the site that is closest to the source. The geometric drainage area a for a particular site $\mathbf{r}_n$ on the network can then be identified with the set of all source sites $\mathbf{r}$ for which the fraction of absorbed walkers is maximized at $\mathbf{r}_n$.
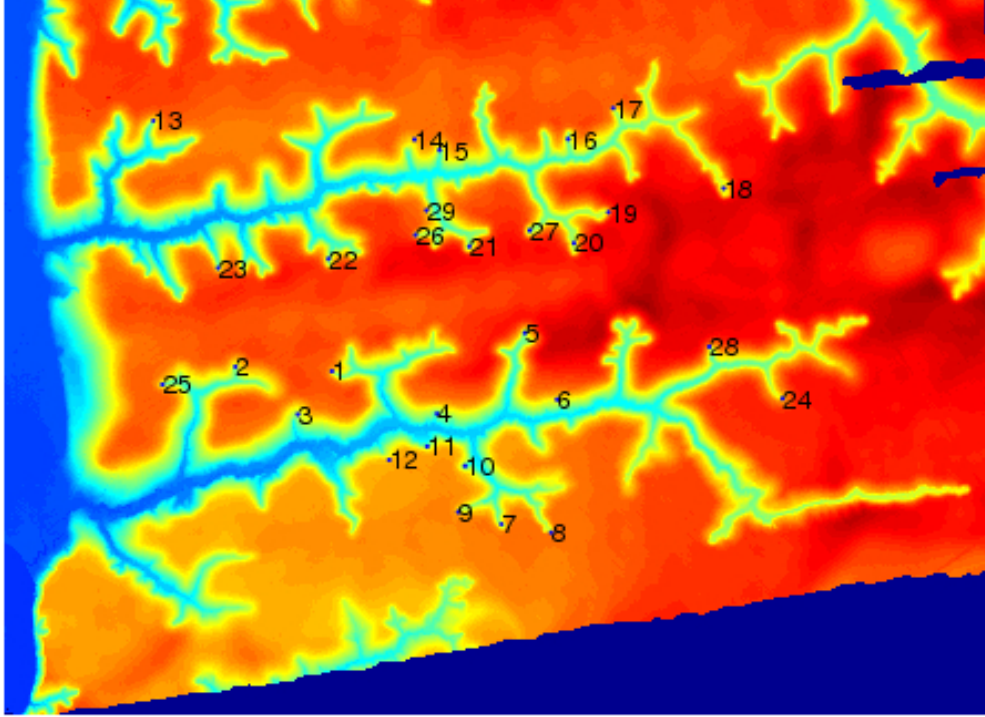
Figure S8: The 29 channel heads analyzed to produce the curvature-area relation in Figure 3c of the main text. Channels were chosen to include a wide variety of drainage areas, including recently formed stubs (e.g. channel head 29, which corresponds to the small-curvature (blue) profile in Figure 3b of the main text) and large channels (e.g. channel head 8, which corresponds to the high-curvature red channel in Figure 3b). Since there is greater uncertainty in the geometric drainage area for recently bifurcated tips, only isolated channels were analyzed.

5 The curvature-area relation

To determine the curvature-area relation in Figure 3c of the main text, we estimated the radius of curvature of the upper-slope convexity (the valley lip) for the 29 channel heads labeled in Figure S8. We calculated the curvature from the first and second derivatives of the longitudinal profiles. (Two examples are shown in Figure 3b.) First, the lower boundary of the lip was identified recursively by fitting a line to the section of the profile that extends from the base of the valley head (i.e., the spring) to the lip. Lines were fit to both an initial segment and the seven meters above that segment. If the slope did not change in the seven meters past the end of the initial segment, the length of the initial segment was increased by one meter and the process was repeated. The slopes were deemed different when their estimated values could be distinguished with greater than 95% confidence. The upper extremity of the lip was found similarly by fitting lines to the flat plain between channels. This scheme resulted in first derivatives h' at two longitudinal coordinates x_1 and x_2, and also the second derivative $h'' = [h'(x_2) - h'(x_1)]/(x_2 - x_1)$. The curvature r^{-1} was then calculated according to its definition,

$$r^{-1} = \frac{h''}{(1 + h'^2)^{3/2}}. \tag{S8}$$

S11

Each measure of curvature was then paired with the geometric drainage area associated with the same channel head. Results are tabulated in Table S1. Because the geometric drainage area is sensitive to tip position when channels are close together, only isolated channels were analyzed. This strategy also helped insure the statistical independence of the measurements.

Table S1: The area, curvature and the direction of growth (bearing, in degrees from north) for each tip is provided. The numbering scheme corresponds to the labels in Figure S8.

Number	Area (km^2)	curvature (m^{-1})	bearing
1	0.038	0.0140	295
2	0.071	0.0210	7
3	0.020	0.0049	19
4	0.028	0.0065	7
5	0.078	0.0170	6
6	0.033	0.0059	351
7	0.042	0.0280	134
8	0.220	0.0870	127
9	0.072	0.0130	251
10	0.022	0.0140	244
11	0.025	0.0160	173
12	0.033	0.0095	135
13	0.036	0.0071	35
14	0.022	0.0030	8
15	0.017	0.0055	353
16	0.024	0.0150	5
17	0.071	0.0150	325
18	0.200	0.0320	165
19	0.089	0.0160	65
20	0.078	0.0430	184
21	0.063	0.0310	188
22	0.049	0.0310	182
23	0.038	0.0210	183
24	0.074	0.0044	110
25	0.065	0.0180	252
26	0.041	0.0230	258
27	0.049	0.0290	222
28	0.096	0.0140	345
29	0.012	0.0098	159

6 Reconstruction of network growth

6.1 Identification of the network

To convert the full three dimensional topographic map to a simplified two-dimensional planform network, we first found a channel "backbone" as follows:

1. We calculated potential flow lines (perpendicular to contours) beginning at a contour near the elevation of the flat plain, and then selected points with a flow line density greater than a given threshold to define the rough backbone. The threshold was chosen so that the channel network tips appeared at a position consistent with our field observations.

2. The rough backbone network was converted to a logical tree structure through a recursive algorithm. Starting from the root, we followed each branch until we reached a tip or bifurcation point. If a tip was reached, the branch was closed. If a bifurcation point was reached, then a new branch was initiated for each stream meeting at that point. We dubbed this a "quick tree" because it could be calculated in $\mathcal{O}(N)$ time, where N is the number of points in the rough backbone.

3. The quick tree was refined and converted to a standard river network format by joining each root stream to the longest channel bifurcating off of it. All streams of length shorter than a given threshold were pruned. This resulted in a center-lined backbone network representing the significant channels in our initial map.

6.2 Backwards evolution

The channel trunks located on the periphery of our high-resolution map (Figure 1 of the main text) were taken as fixed boundaries in the reconstruction. In the southeast, we drew an artificial boundary to represent the effects of a nearby swamp and a change in subsurface properties. The reconstruction appears to be insensitive to the details of where the fixed boundary is chosen.

We used the linear relationship, $v_i = \beta a_i$ (see main text) to evolve the ith channel ($i = 1 \ldots N$) of the backbone network backwards in time. The constant of proportionality β was initially unknown but assumed to be constant. At each time step we

- Find all tips i in the given network.

- Find the geometric drainage area a_i draining into each tip. Each a_i includes drainage to any point within a given distance d from the exact tip. We chose $d = 15$ m to match the physical dimensions of typical channel heads observed in the field.

- Calculate time step as $\mathrm{d}t \propto (\max(a_i))^{-1}$ such that the maximum distance moved by any tip is less than the grid spacing size.

- Retract each tip i by a length $\mathrm{d}x_i = \beta a_i \mathrm{d}t$.

References

S1. Claerbout, J. F. *Imaging the Earth's Interior* (Blackwell Scientific Publications, Boston, 1985).

S2. Bear, J. *Dynamics of Fluids in Porous Media* (Dover Publications, New York, 1972).

S3. Polubarinova-Kochina, P. I. A. *Theory of Ground Water Movement* (Princeton University Press, Princeton, NJ, 1962).

S4. Doyle, P. G. & Snell, J. L. *Random Walks and Electric Networks*. Carus Mathematical Monographs No. 22 (American Mathematical Society, Oberlin, OH, 1984).

S5. Redner, S. *A Guide to First-Passage Processes* (Cambridge University Press, Cambridge, UK, 2001).